European Rotorcraft Forum

THE VORTEX RING STATE OF A SHROUDED ROTOR.

D.J. Pickles*, D. Zagaglia, R.B. Green, A. Busse
University Of Glasgow, UK

* e–mail: david.pickles@glasgow.ac.uk

Abstract
An experimental investigation into the flow field produced by a shrouded rotor, operating in axial descent is presented. Laser Doppler Anemometry (LDA) was used to determine the induced velocity of the rotors, whilst Particle Image Velocimetry (PIV) was applied to investigate the dynamics of the unsteady flow field produced. Tests were repeated using the same rotor, without the shroud, to assess its influence on the observed phenomena. At low descent velocity ratios, the mean flow field resembled that produced by a shrouded rotor operating in hover. At slightly higher descent velocity ratios, the wake from the shrouded rotor broke down, leading to the formation of a large region of recirculation outboard of the shroud which aperiodically sheds into the free stream. Further increases in descent velocity lead the centre of recirculation to form around the external surface of the shroud. The flow topology appears to be generally similar to the one arising from an isolated rotor operating in descent flight, however the results suggest that the presence of the shroud might slightly delay the onset of the Vortex Ring State (VRS).

Keywords: Rotorcraft, Shroud, Aerodynamics, Vortex Ring State, Particle Image Velocimetry (PIV), Laser Doppler Anemometry (LDA), Wind Tunnel.

1. INTRODUCTION

Shrouded rotors have been extensively used in the rotorcraft industry owing to the inherent safety[1] and potential static performance improvements of the design when compared to an isolated rotor[2]. Examples of their application include auxiliary propulsion for compound helicopters, helicopter tail rotors and more recently vertical take off and landing (VTOL) unmanned aerial vehicles (UAVs)[3]. To date, research involving shrouded rotors has mainly focused on characterising the effect shroud design parameters, such as the blade tip clearance[2,4], inlet lip radius[5,6] diffuser length[7], angle and expansion ratio, have on the performance and the structure of the flow field produced by shrouded rotors operating in hover and edgewise flight[8]. However, there is a distinct lack of detailed experimental or numerical data related to shrouded rotors operating in axial descent, despite the fact that this represents an important phase of the flight envelope of UAVs especially when operating in urban environments. In axial descent rotors can experience a flow phenomenon known as the vortex ring (VRS)[9]. When operating in axial descent the vortex system trailed from a rotor, can collapse forming a highly unsteady vortex ring of a similar scale to that of the rotors diameter. The build up and subsequent shedding of the vortex ring occurs over a number of rotor revolutions. Shedding of the vortex ring from the rotor leads to large unpredictable thrust oscillations, increase in rotor torque and the loss of control efficiency characteristic of rotorcraft operating in the VRS.

The mechanism by which the trailed vortex system collapses into the toroidal form associated with the VRS is based on the linear stability analysis of helical vortex filaments performed by Gupta and Loewy (1974)[10] and Widnall (1972)[11] along with the free wake simulations of helicopter rotors operating in axial descent conducted by Bhagwat and Leishman (2000)[12], Leishman et al. (2004)[13] and Ananthan and Leishman (2006)[14]. These investigations showed that the wake from a hovering rotor is inherently unstable. The small geometric perturbations to the helix, with wavelengths equal to a few core diameters or over several helix diameters identified by Gupta and Loewy (1974)[10], and the mutual-

inductance instability of helical vortices identified by Widnall (1972)[11] lead to the breakdown of the helical structure. Typically, this occurs some distance away from the rotor, however, in descending flight this occurs in the vicinity of the rotor[15]. Free-wake simulations performed by Bhagwat and Leishman (2000)[12], Leishman et al. (2004)[13] and Ananthan and Leishman (2006)[14] identified the mutual-inductance instability as the mechanism responsible for the bundling of vortex filaments into rings, which move towards the rotor as it approaches the VRS. Planar smoke flow visualisation of a rotor performed by Stack et al. (2005)[16] identified leapfrogging of vortex filaments as the mechanism responsible for the bundling of the vortex filaments. However, it was shown numerically that the mutual inductance instability can result in the entanglement of helical vortices[17,18,19] which would appear like the vortex pairing of vortices, identified by Stack et al. (2005)[16] on a two dimensional plane. Outboard of the rotor this leads to the build up of vorticity around the rotor blade tips[20]. The build up and subsequent shedding of the recirculation is responsible for the large thrust fluctuations associated with rotors operating in the VRS. Ahlin (2007)[17] indicated that the breakdown of the blade root system is responsible for the formation of the saddle point and the conical region of reverse flow which penetrates towards the rotor disk plane[21].

As previously stated, despite the dangers associated with such flight conditions, there is a distinct lack of detailed experimental or numerical data related to shrouded rotors operating in axial descent Therefore an investigation has been designed to assess if and how the presence of the shroud affects the development of the vortex ring state. To this end, LDA and PIV were used to investigate the flow for a range of descent velocities and results were compared with those obtained without the shroud. Time-averaged data was used to assess the general structures of the flow fields whilst instantaneous snapshots and modal analysis (Proper Orthogonal Decomposition POD) highlighted the unsteady features of the flow.

2. EXPERIMENTAL SETUP

The flow field produced by a $0.1778m$ diameter, two bladed, twisted, tapered, fixed pitch, unarticulated rotor mounted inside a shroud, operating in axial descent was investigated. A schematic diagram of the shrouded rotor is presented in figure **??**. In order to allow the influence of the shroud on the flow field to be characterised, the flow field produced by the unshrouded rotor was also investigated. The fi-

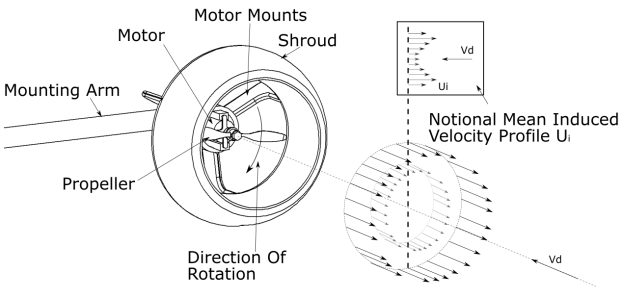

Figure 1: Schematic diagram of the shrouded rotor installed in the DeHavilland wind tunnel.

breglass rotor was lightly loaded and therefore was assumed to be rigid. An AXI-2820/12-V2 brushless motor, mounted on a stand located inside the wind tunnel was used to power the rotor. The shroud was connected to the motor using three support struts located on the inlet side of the rotor, as shown in Figure 1. The rotor was operated at a constant rotational frequency of $66.3 \pm 1Hz$, producing a rotor tip speed of $V_{tip} = 37m/s$ and a blade tip Reynolds number of 15,000. The motors and propellers chosen were all commercial components readily available from most UAV drone retailers.

The shroud, shown in figure 2, was 3D printed out of Prototyping PLA (FDM), and was designed based on the investigation performed by Pereira et al. (2008)[22] to optimise the hovering performance of the shrouded rotor. The shroud had an inlet lip radius of $r_{lip} = 0.02m$, a blade tip clearance ($\delta_{tip} \approx 0.001m$), a diffuser angle $\theta_d = 10^o$, and a diffuser length of $L_d = D_t/2 = 0.089m$. The rotor disk plane was located at the throat of the shroud. A schematic diagram of the shrouded rotor installed in the wind tunnel is shown in figure 1. The shrouded rotor was orientated to induce velocity (U_i) against the wind tunnel, so that the wind tunnel speed (V_d) represented the descent velocity of the shrouded or unshrouded rotor.

A Cartesian (x,y,z)-coordinate system, with its origin at the geometric centre of the shroud outlet plane, is defined so that the y-axis is vertically upwards and the x-axis is orientated against the direction of the wind tunnel's free stream. The counterflow was produced using the University of Glasgow, DeHavilland wind tunnel. This atmospheric closed return, low speed wind tunnel is capable of achieving speeds of up to $|V_d| = 50m/s$ in the $2.65m$ wide by $2.04m$ high octagonal test section with a turbulence intensity below 0.4%. The shrouded and unshrouded rotors were both exposed to a range of descent velocities ranging from $\alpha = (|V_d|/U_i) = 0$ to $\alpha = 2.5$. The test rig

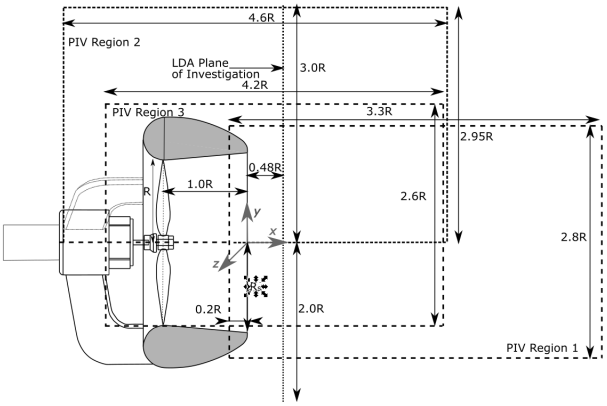

Figure 2: Schematic diagram of the PIV regions of interest and LDA planes investigated for the shrouded rotor in axial descent.

shown in figure 1, had a negligible wind tunnel blockage of 2%. Homogeneous seeding of the wind tunnel for both PIV and LDA was achieved using a Pivtec-GmbH seeder, incorporating 160 Laskin nozzles with a mean olive oil particle substrate diameter of $0.9\mu m$[23].

2.1. LDA

A commercially available Dantec Dynamics two-component Laser Doppler Anemometry (LDA) system was used to investigate the velocity profile produced by both the shrouded and unshrouded rotors $1.48R$ upstream of the rotor disk plane ($x/R = 0.48$), as depicted in figure 2. In hover, measurements were performed on a grid of sample points concentrically spaced around the centre of the rotor to estimate the notional induced velocity U_i, with azimuthal and radial resolutions of 15^o and $0.08R$ respectively. Each of the 289 points were sampled over a period of $10s$. When operating in descent 218 data points along the horizontal and vertical axes of symmetry of the isolated rotor, on both planes of investigation, were sampled for a period of $10s$ with a spatial resolution of $0.08R$. The lasers were both orientated at an angle of 2.5^o coinciding to form a 2.62 x 0.12 x $0.12mm$ measurements volume. The system was operated in burst mode with transit (residence) time enabled to allow for the accurate calculation of the mean flow velocity, and to prevent high velocity bias for high turbulent flows[24 25 26]. The accuracy of the mean flow field was calculated to be $\pm 0.01ms^{-1}$ which corresponds to 0.2% of the rotors peak induced velocity. The location of the measurement volume in the flow field was controlled using a Dantec 9041T3332 3D traverse system which is capable of scanning a measurement volume with a positional accuracy of $\pm 0.01mm$. Figure 2 shows the location of the LDA measurement planes investigated.

2.2. PIV

Two component PIV in the symmetry plane along the longitudinal centre line of the rotor was performed in order to assess the structure of the flow field. A $532nm$ wavelength Litron double cavity oscillator amplified Nd:YAG laser with an output energy of $100mJ$ per pulse was used to deliver the light sheet. A Phantom V341 digital high speed 4 Megapixel camera with a 2560 X 1600 pixel CMOS sensor fitted with a Samyang $135mm$ focal length was used to acquire the raw images. The flow field produced by the shrouded rotor was split into two distinct regions: Region 1: Shroud Outlet; Region 2: Around the Shroud, as shown in figure 2. A single region of interest (Region 3), presented in figure 2, was used to investigate the flow field produced by the unshrouded rotor. The magnification factor (M) of the regions of interest varied from $6.1pixel/mm$ to $6.9pixel/mm$. Three sets of 600 image pairs were recorded at a frequency of $200Hz$ for a range of counterflow velocities for each of the regions of interest investigated. A time delay of $\Delta t = 200\mu s$ was used for all experimental configurations investigated.

Post processing of the raw PIV images (n) was completed using the commercially available software $Davis$ V8.2. PIV of image regions closer than $0.004m$ to the solid surface of the shroud were unreliable as a result of glare, therefore measurements were only made to within $0.005m$ of the shroud surface. The results presented in this paper were produced using a multi-pass cross correlation algorithm with interrogation windows of 48 x 48 pixels with a 50% overlap, followed by an interrogation window of 24 x 24 pixels with a 50% overlap. The resolution of the PIV was approximately $0.002R$ x $0.002R/pixel$ for all regions of interest. The uncertainty of the velocity measurements was estimated to be approximately $\epsilon_u = 0.08ms^{-1}$ for each of the interrogation regions[27]. A maximum displacement error of 0.1 pixels was assumed for each of these PIV regions, owing to sub-pixel interpolation. The unsteadiness of the flow field was assessed by calculating the root mean square (RMS) of the fluctuations of the measured axial velocity.

3. RESULTS

3.1. Characterisation of the mean flow field produced by a shrouded rotor operating in hover.

The flow field produced by the isolated and shrouded rotors operating in hover was characterised using LDA in order to estimate the averaged induced velocity across the rotor disk plane at the shroud outlet.

The mean axial velocity component (u) in a cross-stream plane $0.48R$ upstream (with respect to the wind tunnel flow direction) of the shroud outlet plane is presented in figure 3. Based on the axial velocity profile generated by the shrouded rotor, a notional induced velocity $U_i = 3.3ms^{-1}$ was calculated using equation 1, where u is the time averaged induced velocity at the shroud outlet plane and A_i is the area of the region investigated using LDA.

$$U_i = \frac{\int_0^{1.1R} 2\pi urdr}{A_i} \quad (1)$$

The notional induced velocity of the shrouded rotor was used to scale the descent velocity of both the isolated rotor and the shrouded rotor ($\alpha = |V_d|/U_i$). The same process was used to calculate the induced velocity ($U_{i_R} = 3.8ms^{-1}$) of the isolated rotor on a plane $0.48R$ from the rotor disk plane.

LDA velocity profiles along the vertical (y) axis of symmetry of both the unshrouded and shrouded rotor on a plane $x = 0.48R$ from the shroud outlet plane are presented in figure 4. Analysis of figure 4 shows that the mean axial velocity profile produced by the shrouded rotor is topologically similar to that produced by the isolated rotor, with a region of low velocity flow air surrounded by a ring of high velocity air. The results show that the shroud used in this investigation does not significantly affect the mean axial velocity profile produced by the rotor. Earlier investigations into the flow field produced by a shrouded rotor[28], identified a region of reverse flow underneath the rotor's centre body. This region of reverse flow is not observed in the mean flow field presented in figure 3 or the LDA velocity profiles presented in figure 4. The absence of a rotor centre body inside of the shroud is believed to be responsible for this variation of the mean velocity profile.

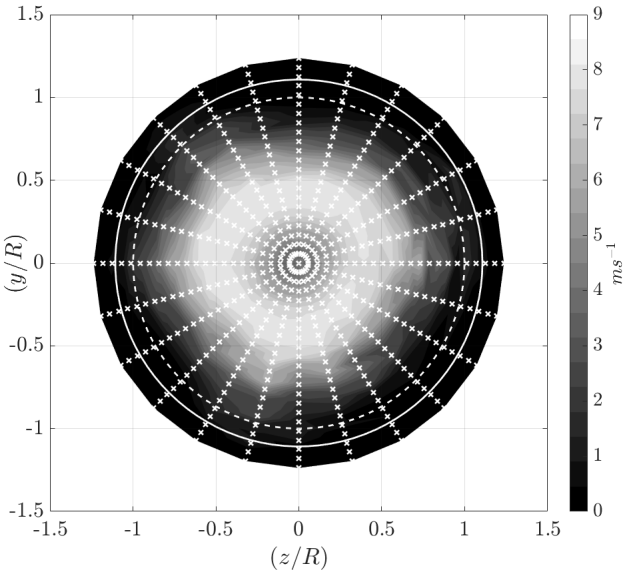

Figure 3: Averaged axial velocity component (u) produced by the shrouded rotor operating in hover $0.48R$ from the shroud outlet plane $(x/R = 0.48)$. This figure was produced using LDA and each sample point location is displayed by a white cross. The rotor blade tip path $--(white)$ and the shroud outlet lip $-(white)$ have been projected onto the plane of investigation.

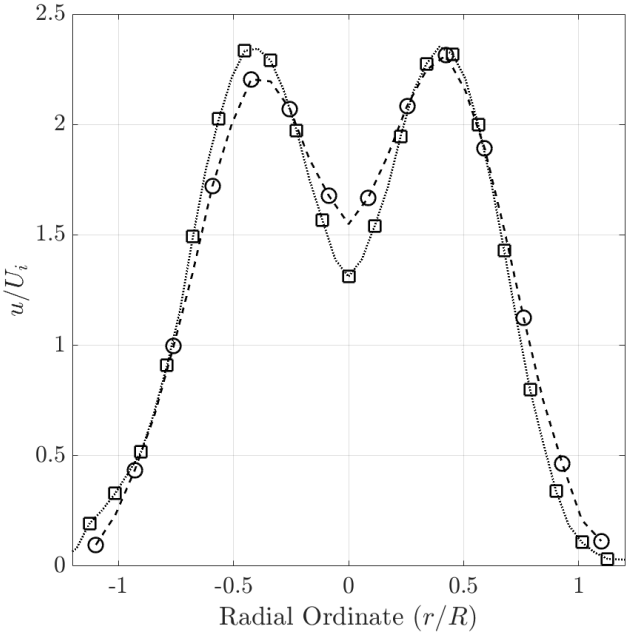

Figure 4: LDA velocity profiles along the horizontal and vertical axes of symmetry of the shrouded and unshrouded rotor $1.48R$ from the rotor disk plane $(x/R = 0.48)$.

3.2. Characterisation of the mean flow field produced by a shrouded rotor operating in axial descent.

Figure 5 shows the development of the mean axial velocity profile produced by the isolated and the shrouded rotor on a plane $1.48R$ from the rotor disk plane $x/R = 0.48$, as the descent velocity ratio was increased from $\alpha = 0$ to $\alpha = 2.0$. At low velocity ratios ($\alpha < 1.2$), the mean axial velocity profile of the isolated rotor developed to resemble that of a round jet, with a single peak velocity located at the centre of the rotor[29] ($y/R = 0$). At higher velocity ratios, the peak axial velocity reduced until the axial velocity profile becomes negative ($-u$) indicating that the interaction between the rotor wake and the wind tunnel free stream occurs downstream of the plane of investigation ($x/R < 0.0$). This indicates that the wind tunnel free stream penetrates through the plane of investigation.

From figure 5, it is clear that, at velocity ratios below ($\alpha = 1.2$), the velocity profile produced by the shrouded rotor is similar to that produced by the unshrouded rotor on this plane of investigation. As the velocity ratio was increased from $\alpha = 0.4$ to $\alpha = 0.9$, the mean axial velocity profile becomes uniform across a large portion of the shroud outlet plane ($y/R \leq |0.4|$). No significant effect could be observed in the mean axial velocity profile across the shroud outlet plane ($y/R \leq |1.0|$), when the descent velocity ratio was increased from $\alpha = 0.4$ to $\alpha = 1.2$. Starting from $\alpha = 1.2$ the profiles of the unshrouded rotor flatten at a faster rate than those of the shrouded rotor, suggesting that the shroud might slightly delay the onset of the VRS. A further increase in the descent velocity leads to a reduction in the mean axial velocity across the shroud outlet plane. At a velocity ratio of $\alpha = 1.4$, the mean flow across the shroud outlet plane is negative ($-u$), indicating that the wind tunnel free stream passes through the plane of investigation.

Figure 6 and figure 7 show the development of the mean flow fields around the isolated and shrouded rotor, as the descent velocity was increased from hover ($\alpha = 0$) to $\alpha = 1.4$. The results presented in figure 6 related to the mean flow field produced by an isolated rotor operating in axial descent were similar to those presented by Green et al. (2005)[21], and display the characteristic features associated with a rotor operating in axial descent. As expected from the LDA results presented earlier, the mean flow field produced by the rotor is topologically similar to that produced by the shrouded rotor when they were both operating in hover, with a region of low velocity air surrounded by a ring of higher velocity air. Mean flow streamlines, calculated using a forward Euler prediction algorithm were used to highlight specific features of the flow field. The results presented in figure 6 show that, at low descent velocities, the near flow field produced by a isolated rotor is similar to that produced by a hovering rotor. As the descent velocity increased, the rotor wake was increasingly encroached upon by the wind tunnel free stream. At the interaction between the rotor wake and the wind tunnel free stream, a saddle point forms in line with the rotor hub. Analysis of figures 6(B) and 6(C) shows that the saddle point moves towards the rotor disk plane as the descent velocity increases. It is hypothesised that, at low descent velocities, the interaction between the rotor wake and the wind tunnel free stream will occur outside of the region of investigation ($x/R > 2.0$). At higher descent velocity ratios a conical region of reverse flow penetrates up to the rotor disk plane. Outboard of the rotor a large region of recirculation forms. As the descent velocity was increased, the recirculation moves from below the rotor, shown in figure 6(C) to above the rotor disk plane, figure 6(d) until the rotor enters the windmill brake state.

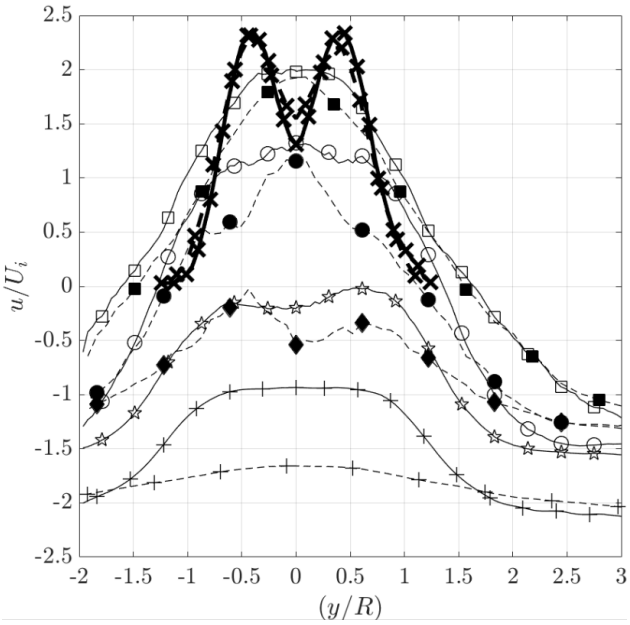

Figure 5: Selective comparison of the mean LDA velocity profiles along the vertical axis of symmetry of the shrouded and unshrouded rotor, on a plane $1.48R$ from the rotor disk plane ($x/R = 0.48$), as the descent velocity was varied from $\alpha = 0$ to $\alpha = 2.0$.

The mean flow field produced by the shrouded rotor exhibits the same general topological features that were discussed above for the unshrouded rotor (see figure 7). At low descent velocities, $\alpha \leq 1.0$ a large region of recirculation forms outboard of the shroud. As the descent velocity increased, the recirculation moved from upstream of the shroud, as shown in figure 7(B) to around the side of the shroud, as shown in figure 7(C). At velocity ratios greater than $\alpha \geq 1.4$ the recirculation is transported downstream, away from the shrouded rotor, as shown in figure 7(D). As with the isolated rotor, at the interaction between the shrouded rotors wake and the wind tunnel free stream a mean flow saddle point forms on the geometric centreline of the shroud. The mean location of the saddle points, extracted from the centreline axial velocity profiles of the PIV images presented in figure 6 and figure 7 are presented in figure 8. Analysis of figure 8 shows that saddle points produced by both the shrouded and unshrouded rotor wakes' interaction with the free stream flow move towards the shroud outlet plane, or the rotor disk plane as the descent velocity was increased. In particular, at every descent velocity, the saddle point appears to be closer to the rotor disk plane for the unshrouded configuration when compared to the shrouded one. This suggests that the overall development of the VRS is slightly delayed by the presence of the shroud, as previously inferred from the LDA data presented in figure 5.

It was only possible to determine the location of the saddle point when it entered the interrogation area. Consequently at velocity ratios less than 0.9 the location of the saddle point could not be determined and thus the relationship between the location of the saddle point and α could not determined for the shrouded or unshrouded rotor configurations from this investigation.

Further analysis of the PIV results revealed that, as with the results of Green et al.[21], the instantaneous PIV snapshots of the flow field produced by both the shrouded and unshrouded rotors differ considerably from the mean flow fields presented earlier in figure 7 and figure 6. Contour plots of the RMS of the fluctuations of the local axial velocity about the local mean axial velocity component for the shrouded rotor (PIV Region: 2) are presented in figure 9.

Note the RMS of the fluctuations is scaled with respect to the notional induced velocity of the shrouded rotor U_i. From figure 9 it is clear that in hover, the unsteadiness of the wake produced by the shrouded rotor is concentrated into a single region located inline with the lip of the shroud, with fluctuations in the order of 40% of the induced velocity. For isolated rotors this unsteadiness occurs as a result of the passage of the blade root and tip vortices, an example of which is shown in figure 10. However, no clear helical vortex structures can be observed in the instantaneous vorticity plots of the wake of the shrouded rotor presented in figure 11. The vorticity component normal to the investigated plane, $(w_z = \frac{\delta u_y}{\delta x} - \frac{\delta u_x}{\delta y})$ presented in figure 10 and figure 11 was calculated using a least square method, which incorporated a weighted differential from four adjacent points in the x and the y direction, in accordance with the method described by Raffel et al. (2007)[27]. The unsteadiness is therefore associated with the shear layers produced by the shrouded rotor wake interacting with the quiescent surroundings. When operating in axial descent, at a velocity ratio of $\alpha = 1.0$ the RMS of the fluctuations is concentrated at the location of the interaction of the wake with the free stream flow. At this location the unsteadiness is of a similar magnitude to the induced velocity, which is much greater than in the wind-off case.

To provide further insight into the dominant structures of the flow field responsible for this unsteadiness Proper Orthogonal Decomposition(POD) by single value decomposition of the individual PIV snapshots of the flow field produced by the shrouded rotor was performed in accordance with the mothod summarised by Taira et al. (2017)[30]. Each PIV snapshot, of a sequence of n snapshots consists of a uniform grid of discrete velocity components of size $\eta_\eta \times \eta_\varepsilon$. The two velocity components were separated into individual matrices of size $\eta_\eta \times \eta_\varepsilon$ before being recombined to form a column vector $f(t_k)$ of size $2\eta_\eta\eta_\varepsilon$. Matrix (F) is then produced by combining the column vectors $f(t)$ together $F = [f(t_1), f(t_2), f(t_3), ...f(t_n)]$. In POD, the matrix (F), which contains the individual velocity components of each instantaneous PIV image pair, is decomposed into a set of orthonormal basis functions, using single value decomposition, that represent the flow field in the most 'optimal' way $(F = \Phi\Sigma\Psi)$. Matrices Φ and Ψ contain the left and right singular vectors of F, and matrix Σ contains the singular values along its leading diagonal. When referring to POD analysis, 'optimal' is used to describe the relative contribution of a given POD mode to the overall kinetic energy of the flow structures. That is, large energetic flow structures that systematically appear in the flow field are captured in the first few POD modes. Summation of the generated modes allow the mean flow field to be reconstructed from the POD modes as well as the reconstruction of individual velocity flow fields. In order to evaluate the importance of each POD mode on individual velocity fields, an analysis of the temporal

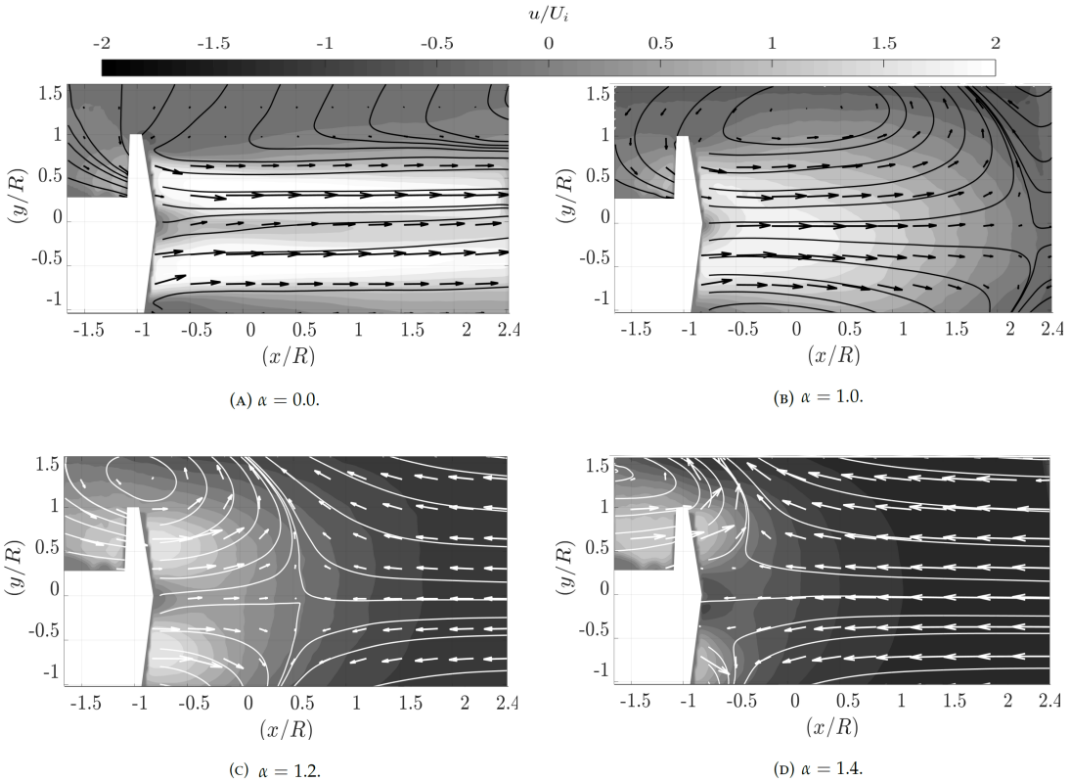

(A) $\alpha = 0.0$. (B) $\alpha = 1.0$.

(C) $\alpha = 1.2$. (D) $\alpha = 1.4$.

Figure 6: Averaged axial velocity contours and streamlines close to the unshrouded rotor for increasing descent velocity $|V_d|$ ($\alpha = [0.0, 1.4]$). Velocity is scaled with respect to the notional induced velocity, (U_i).

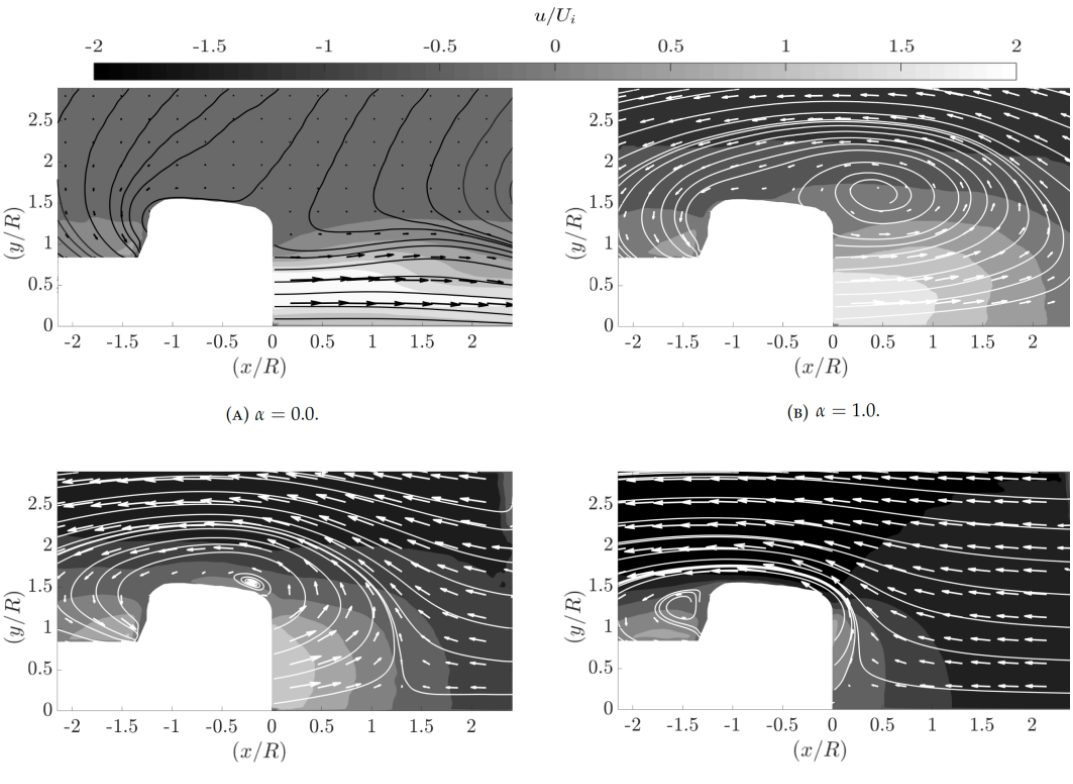

(A) $\alpha = 0.0$. (B) $\alpha = 1.0$.

(C) $\alpha = 1.2$. (D) $\alpha = 1.4$.

Figure 7: Averaged axial velocity contours and streamlines close to the shrouded rotor for increasing descent velocity $|V_d|$ ($\alpha = [0.0, 1.4]$). Velocity is scaled with respect to the notional induced velocity, (U_i).

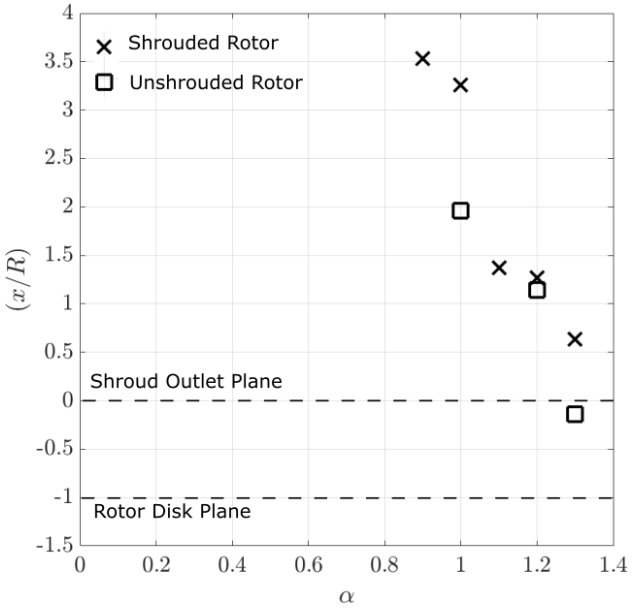

Figure 8: Mean location of the saddle point obtained from PIV measurements of the flow field produced by the unshrouded and the shrouded rotor in axial descent.

coefficients, contained in matrix Ψ associated with each POD mode can be performed. Patter-Rouland et al. (2001)[31] showed that the temporal coefficients of mode $\Psi(n)$ represent the influence mode 'm' has on the development of each instantaneous velocity field (f_n). The influence of each mode on the velocity field was evaluated by subtracting the maximum and minimum reconstructed coefficient forms of the POD mode $\Psi(m)$ from the averaged flow field. The reconstructed flow fields presented in figure 12 show that at a velocity ratio of $\alpha = 1.1$ the unsteadiness of the flow field, presented in figure 12(b,c) is associated with the variation of the wakes penetration into the free stream flow. The location of these fluctuations coincides with the region of high RMS of the axial velocity fluctuations identified in figure 9. Analysis of figure 12 shows that at some velocity ratios the counter flow can penetrate up to the shroud outlet plane, as shown in figure 12(B). The location of the saddle point, identified earlier, varied as a result of the flow fluctuations. The flow fields, produced as a result of the flows fluctuations resemble the two potential flow topologies, produced by a rotor operating in the VRS, previously identified by Green et al. (2005)[21]. The second most energetic mode (not presented in Figure 12 for the sake of conciseness) manifested instead as a radial flapping of the wake. In wind-off conditions, this represented the main source of unsteadiness in the flow field.

4. CONCLUSIONS

An investigation into the structure of the flow field produced by a shrouded and unshrouded rotor operating in hover and axial descent has been performed using Particle Image Velocimetry (PIV) and Laser Doppler Anemometry (LDA). The notional induced velocity of the shrouded rotor's wake, at the shroud outlet plane, was used to scale the descent velocity of both investigations performed.

Data for the shrouded rotor shows that at low descent velocities, $\alpha =< 1.0$ a large region of recirculation forms outboard of the shroud. As the descent velocity increased the recirculation moved from upstream of the shroud to around the side of the shroud, as the rotor enters the VRS. At velocity ratios greater than $\alpha \geq 1.4$ the recirculation is transported downstream, away from the shrouded rotor. The flow topology produced by the shrouded rotor is generally similar to that produced by the isolated counterpart in axial descent. However, the velocity profiles at the shroud outlet plane and the recording of the position of the mean saddle point originating from the interaction between the rotor wake and the wind tunnel free stream suggests that the presence of the shroud might slightly delay the onset of the VRS.

POD showed that most of the flow unsteadiness associated with the VRS is caused by the variation of the wake penetration into the free stream flow. The location of these fluctuations mostly coincides with a region of high RMS of the velocity fluctuation, of the order of the notional induced velocity. In this condition the flow can penetrate up to the shroud outlet plane and the location of the saddle point varied as a result of the flow fluctuations. The flow field evolution resembles that of an isolated rotor operating in the VRS.

ACKNOWLEDGMENTS

The work was funded by the EPSRC. Acknowledgement is given to the National Wind Tunnel Facility, EPSRC Grant Number $EP/L024888/1$, for the provision of experimental equipment.

REFERENCES

[1] L. Young, E. Aiken, J. Johnson, and J. R. D. Andrews. New concets and perspectives on mocro-rotorcraft and small autonomous rotary wing vehicles. *AIAA Applied Aerodynamics Conference, St. Louis* ., 2002.

[2] H. H. Hubbard. Sound measurements of five

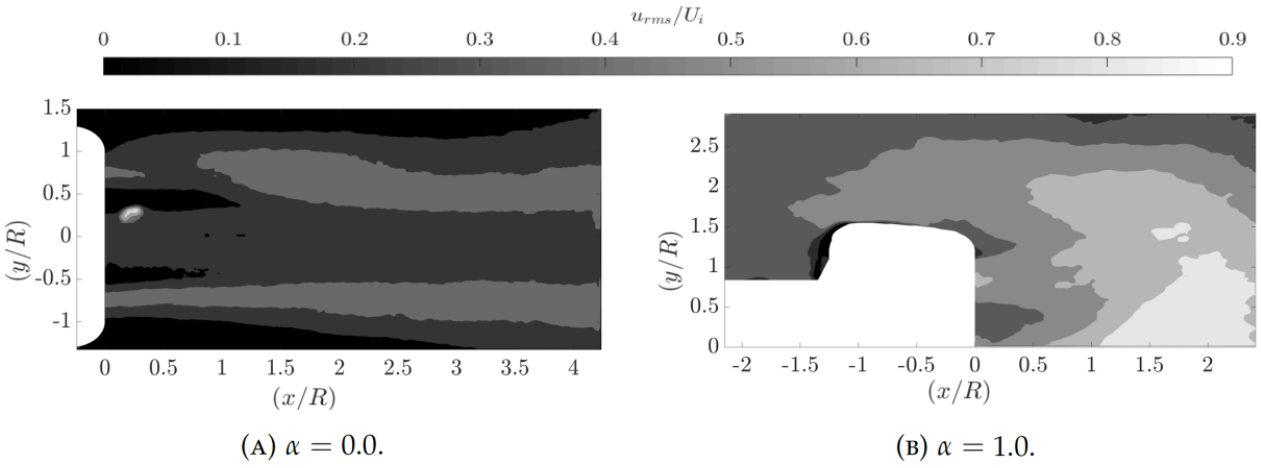

(A) $\alpha = 0.0$. (B) $\alpha = 1.0$.

Figure 9: RMS of the axial velocity components of the flow field produced by the shrouded rotor at a descent velocity ratio of (A) $\alpha = 0.0$ (B) $\alpha = 1.0$.

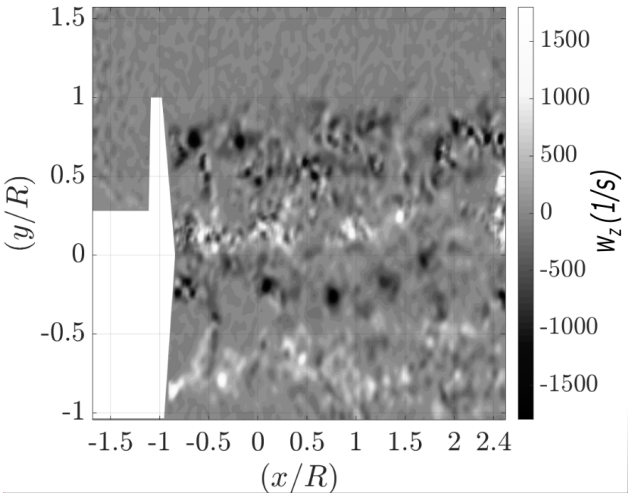

Figure 10: Instantaneous contour plots of the third component of vorticity ($w_z = \frac{\delta u_y}{\delta x} - \frac{\delta u_x}{\delta y}$) contained within the flow field produced by the unshrouded rotor, at a velocity ratio of $\alpha = 0.0$. Note the existence of a system of blade root and tip vortices trailing from the rotor.

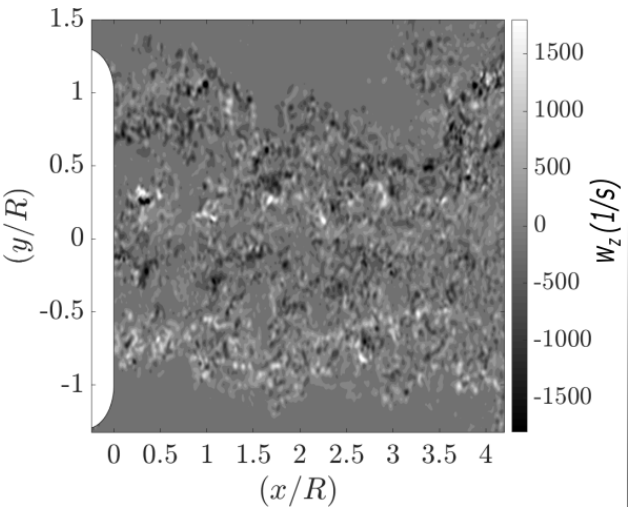

Figure 11: Instantaneous contour plots of the third component of vorticity ($w_z = \frac{\delta u_y}{\delta x} - \frac{\delta u_x}{\delta y}$) contained within the flow field produced by the shrouded rotor, at a velocity ratio of $\alpha = 0.0$.

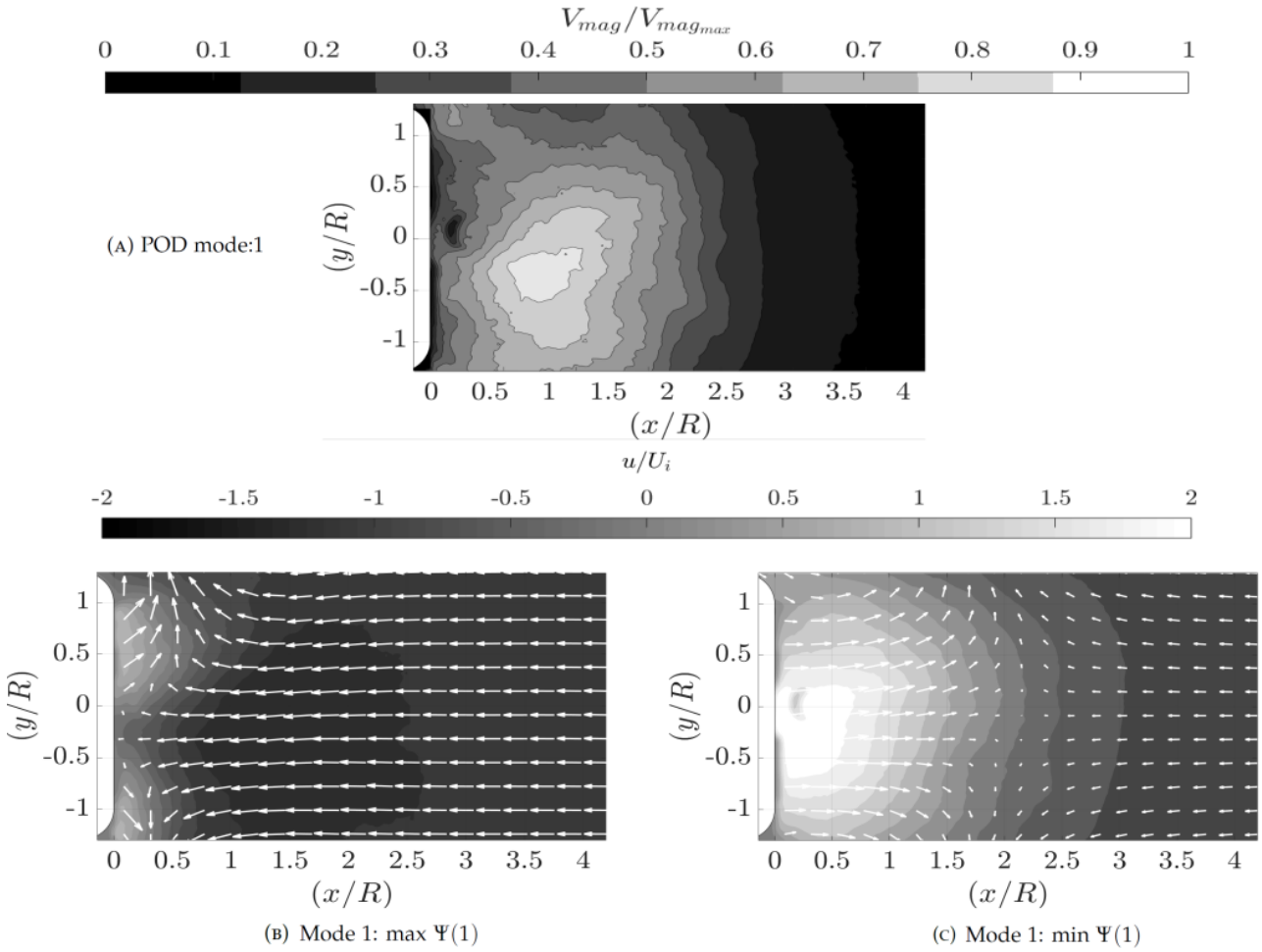

Figure 12: Visualisation of the first POD eigenmodes of the velocity fluctuations produced by a shrouded rotor $\alpha = 1.1$ calculated from 600 instantaneous velocity fields. (A) mode 1. Reconstructed simulations of the velocity field produced by the subtraction of the maximum (B) and minimal (C) reconstruction coefficient representations of the first mode from the mean flow field are presented in this figure. Note: The vector lengths are scaled with respect to the maximum vector length of each individual mode.

shrouded propellers at static conditions. *NACA-TN-2024.*, 1950.

[3] M. Marino, A. Fisher, R. Clothier, S. Watkins, S. Prudden, and C. S. Leung. Rotor wake interactions with an obstacle on the ground. *International Journal of Micro Air Vehicles.*, 7(3):285–299, 2015.

[4] R .T. Taylor. Experimental investigation of the effect of some shroud design variables on the static thrust characteristics of a small-scale shrouded propeller submerged in a wing. *NACA-TN-4126.*, 1958.

[5] W. Krüger. On wind tunnel tests and computations concerning the problem of shrouded propellers. *Tech Report, National Advisory Committee for Aeronautics.*, 1949.

[6] W. Graf, J. Fleming, and W. Ng. Improving ducted fan uav aerodynamics in forward flight. *46th AIAA Aerospace Sciences Meeting and Exhibit.*, page 430, 2008.

[7] D. Black and C. Rohrbach. Shrouded propellers - a comprehensive study. *AIAA 5th Annual Meeting and Technical Display.*, page 994, 1968.

[8] C. Sheng, Q. Zhao, and N. P. Bi. Numerical investigations of ducted fan hover performance for fiw applications. *53rd AIAA Aerospace Sciences Meeting.*, page 1935, 2015.

[9] G. De. Bothezat. The general theory of blade screws. *NACA report no.29*, 1919.

[10] B. P. Gupta and R. G. Loewy. Theoretical analysis of the aerodynamic stability of multiple, interdigitated helical vortices. *AIAA Journal.*, 12(10):1381–1387, 1974.

[11] S. E. Widnall. The stability of a helical vortex filament. *J. Fluid Mechanics.*, 54(4):641–663, 1972.

[12] J. M. Bhagwat and G. J. Leishman. Stability analysis of helicopter rotor wakes in axial flight. *J. American Helicopter Society*, 45(3):165–178, 2000.

[13] G. J. Leishman, M. J. Bhagwat, and S. Ananthan. The vortex ring state as a spatially and temporally developing wake instability. *J. American Helicopter Society.*, 49(2):160–175, 2004.

[14] S. Ananthan and J. G. Leishman. Rotor wake aerodynamics in large amplitude maneuvering flight. *J. American Helicopter Society.*, 51(3):225–243, 2006.

[15] S. Newman, R. E. Brown, J. Perry, S. Lewis, M. Orchard, and A. Modha. Predicting the onset of wake breakdown for rotors in descending flight. *J. American Helicopter Society.*, 48(1):28–38, 2003.

[16] J. Stack, F. X. Caradonna, and O. Savas. Flow visualizations and extended thrust time histories of rotor vortex wakes in descent. *J. American Helicopter Society.*, 50(3):279–288, 2005.

[17] A. G. Ahlin and R. E. Brown. The vortex dynamics of the rotor vortex ring phenomenon. *American Helicopter Society, 63rd Annual Forum, Virginia Beach, Virginia*, 2007.

[18] G. A. Ahlin. *The fluid dynamics of the helicopter vortex ring phenomenon.* PhD thesis. University of London, 2007.

[19] R. E. Brown, A. J. Line, and G. A. Ahlin. Fuselage and tail-rotor interference effects on helicopter wake development in descending flight. *American Helicopter Society, 60th Annual Forum, Maryland*, 2004.

[20] O. Savas, R. B. Green, and F. X. Caradonna. Coupled thrust and vorticity dynamics during vortex ring state. *J. American Helicopter Society.*, 54(2):22001, 2009.

[21] R. B. Green, E. A. Gillies, and R. E. Brown. The flow field around a rotor in axial descent. *J. Fluid Mechanics.*, 534:237–261, 2005.

[22] J. L. Pereira. Hover and wind-tunnel testing of shrouded rotors for improved micro air vehicle design. *PhD. Thesis.*, 2008.

[23] PIVTechGmbH. Pivpart160 product information, 2019. https://www.pivtec.com/, Last accessed on 14/04/2019.

[24] Z. Zhang. *LDA Application Methods: Laser Doppler Anemometry for Fluid Dynamics*. Springer, 2010.

[25] W. K. George. Quantitative measurement with the burst-mode laser doppler anemometer. *J. Experimental Thermal and Fluid Science*, 1(1):29–40, 1988.

[26] H. E. Albrecht, M. Borys, N. Damaschke, and C. Tropea. Laser doppler and phase doppler measurement techniques. *Springer Science and Business Media*, 2013.

[27] M. Raffel, C. Willert, S. Wereley, and J. Kompenhans. *Particle Image Velocimetry, A Practical Guide. Second Edition*. Springer, 2007.

[28] P. Martin and C. Tung. Performance and flowfield measurements of a 10-inch ducted rotor vtol uav. *American Helicopter Society 60th Annual Forum Proceedings, Baltimore*, 2004.

[29] S. Bernero. *A turbulent jet in counterflow.* PhD thesis. Berlin: Technical University Of Berlin, 2000.

[30] K. Taira, S. L. Brunton, S. T. M. Dawson, C. W. Rowley, T. Colonius, B. J. Mckeon, O.T. Schmidt, S. Gordeyev, V. Theofilis, and L. S. Ukeiley. Modal analysis of fluid flows: An overview. *AIAA Journal*, 55(12):4013–4041, 2017.

[31] B. Patter-Rouland, G. Lalizel, J. Moreau, and E. Rouland. Flow analysis of an annular jet by particle image velocimetry and proper orthogonal decomposition. *Measurement Science and Technology*, 12:1404–1412, 2001.